

same effective potential is used to calculate the fusion probability, see below). Approximations had to be introduced: the two neutrons are treated as one cluster, and the model space had to be limited, preventing a calculation at the lowest energy. However, the agreement of the predicted distributions with experimental data (see Fig. 3b) further supports the identification of the transfer process.

The experimental cross-sections for the events in Fig. 3 were calculated as in the case of fission. The detection efficiency depends on the angular distributions, which are not known in the case of the transfer process for such an exotic system. We have used a set of theoretical angular distributions from DWBA calculations in a reduction procedure (fitting the experimental data) to extract the efficiency of each detector, taking into account their geometry. The fusion cross-sections were then calculated as the difference between the total fission and the transfer fission. The resulting data are shown in Fig. 4; the large uncertainty is mainly due to the procedure for the evaluation of the efficiency.

At energies below the barrier, we find experimentally that there is no substantial enhancement of the fusion cross-section for the halo nucleus  ${}^6\text{He}$ . The large observed yield for fission is entirely due to a direct process, the two-neutron transfer to the target nucleus. Other direct processes may also be present, though not detected owing to the fission signature we required. The coupling to these degrees of freedom, as well as the effect of the halo in  ${}^6\text{He}$ , is not sufficient to promote an enhancement of the sub-barrier fusion cross-section.

Breakup has been accounted for by using the effective optical potential derived in the CDCC model of the  ${}^6\text{He}$  breakup. The fusion cross-section (solid line in Fig. 4) was then obtained by employing a short-range imaginary potential to reproduce the incoming-wave boundary condition<sup>12</sup> (the inset in Fig. 4 shows the same for the  ${}^4\text{He} + {}^{238}\text{U}$  system). At the same time, the DWBA calculations provide an estimate of the magnitude of the two-neutron transfer process to excited states in  ${}^{240}\text{U}$  (dotted line). Whereas the agreement for the transfer process suffers from the rough approximations used, the fusion cross-section is well reproduced, corroborating our picture for the processes with the halo nucleus  ${}^6\text{He}$  at energies around the barrier. Still, the grounds for such picture are primarily in the experimental results presented here: a large reaction cross-section, due to direct processes rather than to an enhancement of fusion. □

Received 29 July; accepted 3 September 2004; doi:10.1038/nature02984.

- Caldeira, A. O. & Leggett, A. J. Influence of dissipation on quantum tunnelling in macroscopic systems. *Phys. Rev. Lett.* **46**, 211–214 (1981).
- Tsukada, M., Kobayashi, S. I., Kurihara, S. & Nomura, S. (eds) *Proc. 4th Int. Symp. Foundations of Quantum Mechanics, Tokyo 1992* (Jpn. J. Appl. Phys. Ser. 9, The Institute of Pure and Applied Physics, Tokyo, 1993).
- Stokstad, R. G. *et al.* Effect of nuclear deformation on heavy-ion fusion. *Phys. Rev. Lett.* **41**, 465–469 (1978).
- Austin, S. M. & Bertsch, G. F. Halo nuclei. *Sci. Am.* **272**, 62–67 (1995).
- Dasso, C. H. & Vitturi, A. Does the presence of  ${}^{11}\text{Li}$  breakup channels reduce the cross section for fusion processes? *Phys. Rev. C* **50**, R12–R14 (1994).
- Hussein, M. S., Pato, M. P., Canto, L. F. & Donangelo, R. Near-barrier fusion of  ${}^{11}\text{Li}$  with heavy spherical and deformed targets. *Phys. Rev. C* **46**, 377–379 (1992).
- Tanihata, I. *et al.* Measurements of interaction cross sections and nuclear radii in the light p-shell region. *Phys. Rev. Lett.* **55**, 2676–2679 (1985).
- Hansen, P. G. & Jonson, B. The neutron halo of extremely neutron-rich nuclei. *Europhys. Lett.* **4**, 409–414 (1987).
- Zhukov, M. V. *et al.* Bound state properties of Borromean halo nuclei:  ${}^6\text{He}$  and  ${}^{11}\text{Li}$ . *Phys. Rep.* **231**, 151–199 (1993).
- Beckerman, M. Sub-barrier fusion of two nuclei. *Rep. Prog. Phys.* **51**, 1047–1103 (1988).
- Dasso, C. H., Landowne, S. & Winther, A. Channel-coupling effects in heavy-ion fusion reactions. *Nucl. Phys. A* **405**, 381–396 (1983).
- Rhoades-Brown, M. J. & Braun-Munzinger, P. Explanation of sub-barrier fusion enhancement in a coupled channels model. *Phys. Lett. B* **136**, 19–23 (1983).
- Dasso, C. H., Gaisado, J. L., Lenzi, S. M. & Vitturi, A. Coulomb- and nuclear-induced break-up of halo nuclei at bombarding energies around the Coulomb barrier. *Nucl. Phys. A* **597**, 473–486 (1996).
- Hagino, K., Vitturi, A., Dasso, C. H. & Lenzi, S. M. Role of breakup processes in fusion enhancement of drip-line nuclei at energies below the Coulomb barrier. *Phys. Rev. C* **61**, 037602 (2000).
- Takigawa, N., Kuratani, M. & Sagawa, H. Effect of breakup reactions on the fusion of a halo nucleus. *Phys. Rev. C* **47**, R2470–R2473 (1993).
- Takahashi, J. *et al.* Is fusion inhibited for weakly bound nuclei? *Phys. Rev. Lett.* **78**, 30–33 (1997).
- Canto, L. F., Donangelo, R., de Matos, L. M., Hussein, M. S. & Lotti, P. Complete and incomplete fusion in heavy ion collisions. *Phys. Rev. C* **58**, 1107–1117 (1998).

- Dasgupta, M. *et al.* Fusion versus breakup: observation of large fusion suppression for  ${}^9\text{Be} + {}^{208}\text{Pb}$ . *Phys. Rev. Lett.* **82**, 1395–1398 (1999).
- Hinde, D. J. *et al.* Fusion suppression and sub-barrier breakup of weakly bound nuclei. *Phys. Rev. Lett.* **89**, 272701 (2002).
- Kolata, J. J. *et al.* Sub-barrier fusion of  ${}^6\text{He}$  with  ${}^{209}\text{Bi}$ . *Phys. Rev. Lett.* **81**, 4580–4583 (1998).
- Aguilera, E. F. *et al.* Transfer and/or breakup modes in the  ${}^6\text{He} + {}^{209}\text{Bi}$  reaction near the Coulomb barrier. *Phys. Rev. Lett.* **84**, 5058–5061 (2000).
- Trotta, M. *et al.* Large enhancement of the sub-barrier fusion probability for a halo nucleus. *Phys. Rev. Lett.* **84**, 2342–2345 (2000).
- Vandenbosch, R. & Huizenga, J. R. *Nuclear Fission* 463 (Academic, New York, 1973).
- Ryckewaert, G., Colson, J. M., Gaelels, M., Loiselet, M. & Postiau, N. Recent results from the Louvain-la-Neuve RIB-facility. *Nucl. Phys. A* **701**, 323c–326c (2002).
- Di Pietro, A. *et al.* Reactions induced by the halo nucleus  ${}^6\text{He}$  at energies around the Coulomb barrier. *Phys. Rev. C* **67**, 044613 (2004).
- Tamura, T. Compact reformulation of distorted-wave and coupled-channel Born approximations for transfer reactions between nuclei. *Phys. Rep.* **14**, 59–96 (1974).
- Thompson, I. J. Coupled reaction channels calculations in nuclear physics. *Comput. Phys. Rep.* **7**, 167–212 (1988).
- Kamimura, M. *et al.* Coupled-channels theory of breakup processes in nuclear reactions. *Prog. Theor. Phys. Suppl.* **89**, 1–211 (1986).
- Rusek, K., Keeley, N., Kemper, K. W. & Raabe, R. Dipole polarizability of  ${}^6\text{He}$  and its effect on elastic scattering. *Phys. Rev. C* **67**, 041604 (2003).

**Acknowledgements** R.R. is a Postdoctoral Researcher for the Fonds voor Wetenschappelijk Onderzoek - Vlaanderen. This work has been supported in part by the European Commission Fifth Framework programme on Access to Research Infrastructure.

**Competing interests statement** The authors declare that they have no competing financial interests.

**Correspondence** and requests for materials should be addressed to R.R. (riccardo.raabe@fys.kuleuven.ac.be).

## Metal–insulator–semiconductor optoelectronic fibres

Mehmet Bayindir<sup>1</sup>, Fabien Sorin<sup>2,3\*</sup>, Ayman F. Abouraddy<sup>1\*</sup>, Jeff Viens<sup>1,3</sup>, Shandon D. Hart<sup>1,3</sup>, John D. Joannopoulos<sup>1,2,4</sup> & Yoel Fink<sup>1,2,3</sup>

<sup>1</sup>Research Laboratory of Electronics, <sup>2</sup>Center for Materials Science and Engineering, <sup>3</sup>Department of Materials Science and Engineering, <sup>4</sup>Department of Physics, Massachusetts Institute of Technology, Cambridge, Massachusetts 02139, USA

\* These authors contributed equally to this work

The combination of conductors, semiconductors and insulators with well-defined geometries and at prescribed length scales, while forming intimate interfaces, is essential in most functional electronic and optoelectronic devices. These are typically produced using a variety of elaborate wafer-based processes, which allow for small features, but are restricted to planar geometries and limited coverage area<sup>1–3</sup>. In contrast, the technique of fibre drawing from a preformed reel or tube is simpler and yields extended lengths of highly uniform fibres with well-controlled geometries and good optical transport characteristics<sup>4</sup>. So far, this technique has been restricted to particular materials<sup>5–7</sup> and larger features<sup>8–12</sup>. Here we report on the design, fabrication and characterization of fibres made of conducting, semiconducting and insulating materials in intimate contact and in a variety of geometries. We demonstrate that this approach can be used to construct a tunable fibre photodetector comprising an amorphous semiconductor core contacted by metallic microwires, and surrounded by a cylindrical-shell resonant optical cavity. Such a fibre is sensitive to illumination along its entire length (tens of meters), thus forming a photodetecting element of dimensionality one. We also construct a grid of such fibres that can identify the location of an illumination point. The advantage of this type of photodetector array is that it needs a number of elements

of only order  $N$ , in contrast to the conventional order  $N^2$  for detector arrays made of photodetecting elements of dimensionality zero.

Our approach entails the drawing of extended fibre lengths fabricated by arranging a low-melting-temperature crystalline conductor (Sn), amorphous semiconductors (As–Se–Te–Sn and  $\text{As}_2\text{Se}_3$ ), and high glass-transition-temperature polymeric insulators (polyetherimide, PEI, and polyethersulphone, PES) into a preform which shares the final fibre geometry but lacks functionality owing to the absence of intimate contact and proper element dimensions. The preform is subsequently heated and drawn into a fibre that preserves the initial geometry while forming intimate interfaces and feature sizes down to below 100 nm. This process has led to the creation of two prototypical functional fibre structures that we discuss in detail here: (1) a fibre designed for dual electron-photon transport, and (2) a tunable, narrow-band fibre photodetector.

The fibre for dual electron-photon transport is comprised of a hollow air core, surrounded by an omnidirectional dielectric mirror<sup>13–17</sup> formed from eight pairs of alternating layers of  $\text{As}_2\text{Se}_3$  and PEI (layer thicknesses of 150 and 280 nm, respectively). The refractive indices of  $\text{As}_2\text{Se}_3$  and PEI are 2.83 and 1.65 respectively at 1.5  $\mu\text{m}$ , as measured by using a Sopra GES5 ultraviolet-visible-infrared spectroscopic ellipsometer (see <http://mit-pbg.mit.edu/Pages/Ellipsometry.html>). This multilayer structure provides the optical confinement to the low-index core. Immediately adjacent to this omnidirectional mirror is a circular array of 60 Sn metal strands

with diameters of  $\sim 8 \mu\text{m}$  each (see ‘Preform preparation and fibre drawing’ in Methods). The whole fibre is then surrounded with a PES polymer cladding. An SEM micrograph of the fibre cross-section is shown in Fig. 1a. The optical transport characteristics of the fibre are determined by the positions of the photonic bandgaps. For example, fibres having outer diameters of 980, 1,030 and 1,090  $\mu\text{m}$  have fundamental bandgaps centred at 1.62, 1.75 and 1.85- $\mu\text{m}$  wavelengths, respectively (see Fig. 1c). Optical transmission spectra were determined using a Fourier transform infrared (FTIR) spectrometer (Bruker Tensor 37). The fibre shown in Fig. 1b (1-mm outer diameter) appears green to the eye because of reflection from the third-order bandgap.

We have performed a systematic investigation of the losses incurred upon propagation through simple (non-metal-containing) hollow-core multilayer photonic bandgap fibres in refs 15 and 17. The loss of such fibres for radiation at a wavelength of 10.6  $\mu\text{m}$  was found to be less than 1  $\text{dB m}^{-1}$  (ref. 17). More recently, we have characterized such fibres at a wavelength of 1.5  $\mu\text{m}$ , and measured losses to be approximately 5.5  $\text{dB m}^{-1}$  (ref. 15). The loss mechanisms are found to be (1) radiation through the multilayers, (2) intrinsic materials absorption, (3) nonuniformity in the layer thicknesses, and (4) scattering due to internal surface roughness. Because the light in the electron-photon fibre is very strongly confined within the hollow core by the cylindrical omnidirectional mirror, it is expected that the presence of additional material components or structural complexity lying outside the cylindrical mirror will not significantly affect the losses through this hollow fibre. Indeed, initial loss measurements on the electron-photon transport fibres yield loss levels that are comparable to the cylindrical photonic bandgap fibres of similar structural characteristics. In particular, broad-band FTIR cut-back measurements on electron-photon fibres of 1 m length and core size 800  $\mu\text{m}$  with eight bilayers yielded a transmission loss value of 4.9  $\text{dB m}^{-1}$ , and a bending loss of 0.9 dB for a 90° degree bend with a bending radius of 6 cm. These losses, although higher than those for silica-based holey fibres, are among the lowest reported values for hollow polymer fibres. To examine the electrical properties of the fibre, on the other hand, both ends of the fibre were coated with a thick layer of gold that electrically connects all the Sn wires. The current–voltage characteristics of the 980- $\mu\text{m}$ -thick fibre are displayed in Fig. 1d, showing clear ohmic response.

Whereas the above fibre exhibits both electrical and optical transmission properties, these are spatially separated and indepen-

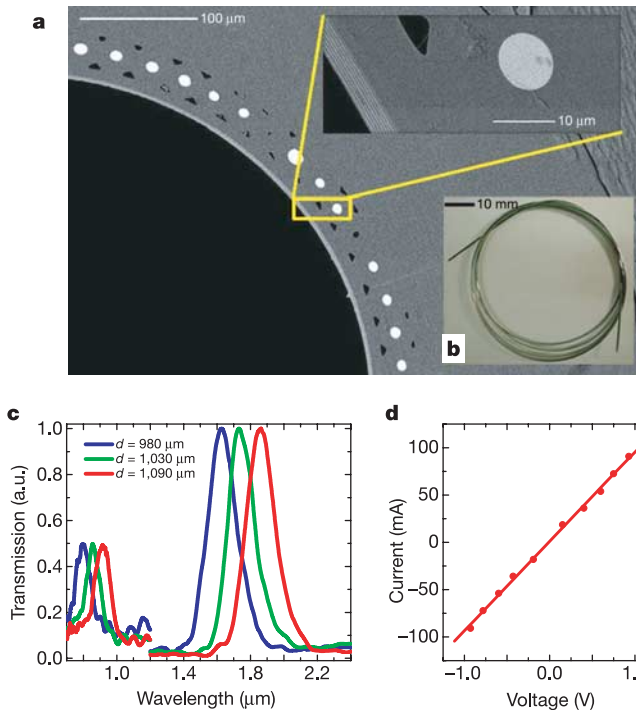


**Figure 1** Dual electron-photon fibre (hybrid fibre). **a**, SEM micrograph of the cross-section of the hybrid fibre with 800- $\mu\text{m}$  hollow core, omnidirectional mirror layers, metallic filament array and polymer cladding. The inset shows eight pairs of quarter-wave  $\text{As}_2\text{Se}_3/\text{PEI}$  multilayers and one of the metallic, Sn filaments in the ring that is surrounding the mirror layers. **b**, Photograph of a 1-mm-thick, 1-m-long hybrid fibre. The fibre appears green to the eye by virtue of reflection from the third-order photonic band gap of the omnidirectional mirror, located at 550 nm. **c**, Normalized transmission spectra of three different fibres, having outer diameters of 980, 1,030 and 1,090  $\mu\text{m}$ . The primary and second-order photonic bandgaps are located at 1.62 and 0.8  $\mu\text{m}$  for the 980- $\mu\text{m}$ -thick fibre, and are shifted to longer wavelengths as the fibre diameter increases. **d**, Measured electrical current along the 980- $\mu\text{m}$ -thick, 15-cm-long fibre as a function of applied bias voltage.

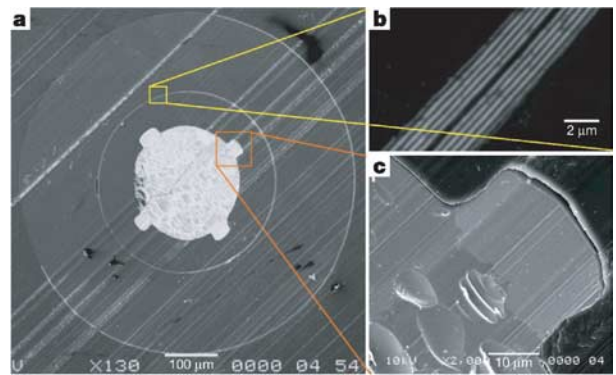


**Figure 2** Integrated optoelectronic device fibre. **a**, SEM micrograph of the entire cross-section of a 650- $\mu\text{m}$ -thick device fibre with a 200- $\mu\text{m}$  chalcogenide glass core surrounded by a PES cladding. The core region is surrounded by a resonant cavity structure (eight pairs of  $\lambda/4$   $\text{As}_2\text{Se}_3/\text{PEI}$  multilayers, with a  $\lambda/2$  resonant cavity in the middle). The bright regions on the polymer–glass interface are the Sn metal electrodes, 18- $\mu\text{m}$  thick and 30- $\mu\text{m}$  wide, which are continuous along the whole fibre length. **b**, A magnified micrograph showing the resonant optical cavity structure. **c**, A magnified micrograph demonstrating the excellent quality of the semiconductor–metal interface.

dent; that is, the propagating electrons and photons do not interact. In our second fibre, we specifically introduce an optoelectronic interaction. This is realized by forming, in the core of the fibre, a photoconductive chalcogenide cylinder contacted with metal electrodes that produces current upon illumination under bias conditions. A single (radial) mode cylindrical-shell optical cavity is introduced in the optical path shielding the photoconducting core from ambient illumination sources. Upon external illumination, when the wavelength of the radiation matches that of the cavity resonance, we observe an electric response from the fibre core, thus establishing the spectroscopic functionality of the fibre.

Figure 2 shows SEM micrographs of the spectroscopic fibre cross-section. The fibre core is  $\text{As}_{40}\text{Se}_{50}\text{Te}_{10}\text{Sn}_5$  (AST-Sn), a highly photoconductive glass, optimized subject to the following requirements (see ‘Glass synthesis’ in Methods): (1) large photoconductivity in the wavelength range of interest; (2) viscosity range compatible with the polymer; and (3) enhanced stability against crystallization during fibre drawing. The core is contacted by four Sn electrodes to form the photodetecting element. An enlargement of the metal–semiconductor interface demonstrating the intimate contact is shown in Fig. 2a. A resonant optical cavity structure is formed by a multilayer made of  $\text{As}_2\text{Se}_3$  and PEI with a  $\lambda/2$  defect layer; an enlargement of the resonant cavity structure is shown in Fig. 2b. The micrograph shown in Fig. 2c demonstrates excellent contact between the semiconducting core and a metal electrode (see ‘Preform preparation and fibre drawing’ in Methods).

To confirm the fidelity of the metal–semiconductor contact and characterize its photoconductive properties, we measured the broad-band photoconductive response of a two-electrode fibre without a multilayer structure (the red curve in Fig. 3a). A 50-V direct current (d.c.) voltage was applied to the fibre and the current was measured using a pico-ampere meter/d.c. voltage source (Yokogawa/Hewlett Packard 4140B). The fibre is illuminated externally with a laser beam from a tunable Optical Parametric Oscillator (OPO). Optical transmission of bulk glass (12-mm diameter and 5-mm length) was determined by an FTIR measurement (blue curve in Fig. 3a). The spectral photoconductive response is commensurate with the optical transmission measurement.

The resonance wavelength and photonic bandgap are both determined by the outer diameter of the device fibre. We fabricated three fibres of outer diameters 870, 890 and 920  $\mu\text{m}$ , which have calculated resonance wavelengths of 1.26, 1.29 and 1.33  $\mu\text{m}$ , respectively. In these fibres, the multilayer structure was situated at the fibre outer surface. The multilayer structure in the three fibres consists of three bilayers,  $\text{As}_2\text{Se}_3$  and PEI, a  $\lambda/2$  PEI cavity, followed by three more bilayers. For the 920- $\mu\text{m}$  fibre, for example, the thicknesses of  $\text{As}_2\text{Se}_3$  and PEI layers are 117 and 204 nm, respectively. The reflectivity of the optical cavity structure was measured for single fibres having these diameters with an FTIR spectrometer and microscope (Nicolet/SpectraTech NicPlan infrared microscope and Magna 860 FTIR spectrometer), and are displayed in Fig. 3b. The FTIR spectra agree well with the calculated spectra. The microscope objective admits a range of angles that vary from normal incidence to 35°, so the observed dip in the reflection spectra is wider and shallower. The cavity resonance shifts slightly in wavelength when the angle of incidence changes. Such a large angular cone, as determined by the microscope objective numerical aperture (NA) of 0.58, leads to an averaging effect that reduces the apparent quality factor of the cavity mode.

To characterize the optoelectronic response of our integrated device fibre, it is useful to measure both the electrical photocurrent and the optical reflectivity simultaneously. We externally illuminated the three aforementioned two-electrode device fibres with the OPO laser beam and measured the back-reflected light through a beam splitter, while simultaneously monitoring the generated photocurrent (see ‘Optical characterization of device fibre’ in Methods).

In Fig. 3c, we display the measurement results of the back-reflected light from three different fibres as wavelength of the laser beam is swept. Concurrently, in Fig. 3d we plot the results of photocurrent measurements of these fibres. At the resonance wavelength, the back-reflection is diminished, and the light reaches the photoconductive core. Consequently, the corresponding photocurrent is enhanced.

These novel fibre structures offer a unique possibility for constructing an optoelectronic functional fabric because the fibres are

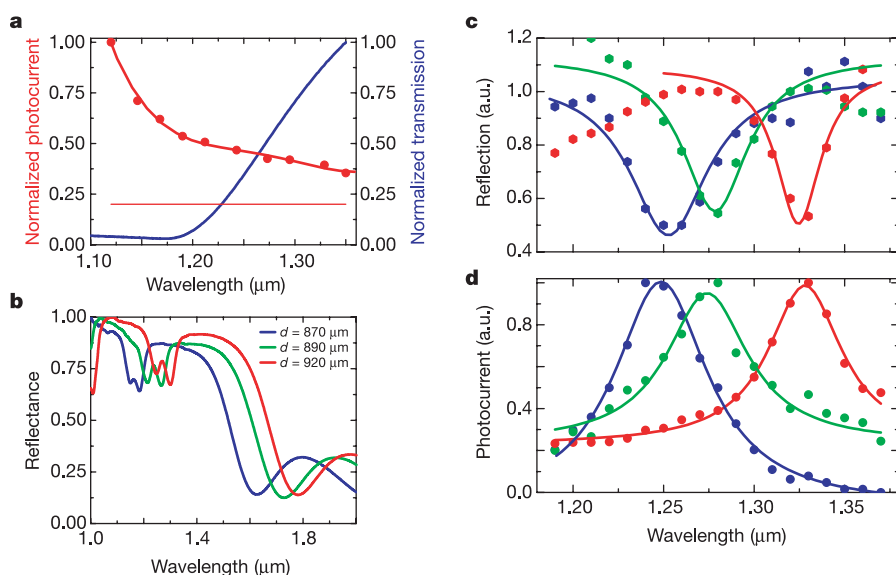


**Figure 3** Results of optical and electrical measurements performed on the device fibres. **a**, The red curve is the normalized electrical current measured when illuminating a 890- $\mu\text{m}$  two-electrode fibre, not equipped with a multilayer structure. The horizontal red line indicates the dark current level. The illumination was derived from a tunable OPO (coherent) and the wavelength was swept while keeping the optical power constant. The blue curve shows the normalized transmission of a bulk AST-Sn glass sample.

**b**, FTIR-measured spectra of device fibres with 870, 890 and 920- $\mu\text{m}$  outer diameter. **c**, Measured back-reflected light power from the same three device fibres when illuminated with a tunable OPO laser beam. **d**, Simultaneously measured photocurrent through the device fibre. Note that at the location of the resonance, the back-reflection is diminished (light is admitted into the fibre and reaches the photoconductive core) while the corresponding photocurrent, consequently, is enhanced.

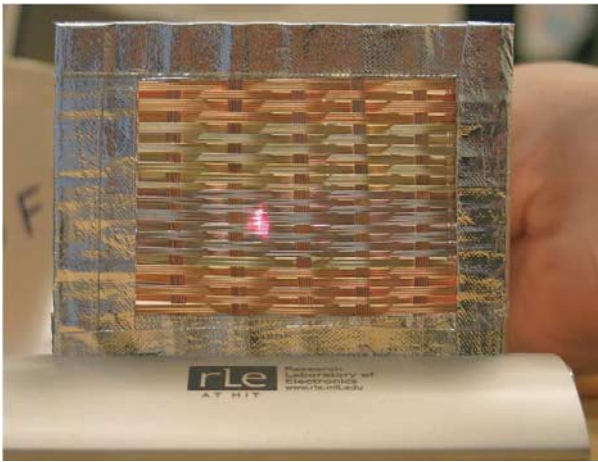


**Figure 4** A woven spectrometric fabric. The fabric consists of interleaved threads, 400 to 500- $\mu\text{m}$ -thick, chosen from our device fibres. The visual appearance of the fabric, specifically the range of exhibited colours, is a result of the tight control exerted over the optical properties of the produced fibres.

both flexible and mechanically tough, and can thus be woven, as shown in Fig. 4. The fibres chosen to be used in this fabric are of slightly different diameters (400–500  $\mu\text{m}$ ), and hence exhibit different bandgap positions, and resonant cavity wavelengths, manifested in their colours (corresponding to primary photonic bandgaps). Furthermore, interesting device applications follow not only from the ability to engineer the single-fibre properties, but also from the specifics of fibre arrangements into larger assemblies. For example, in constructing a two-dimensional optical detector array, a desired resolution of  $N \times N$  pixels per unit area would require  $N^2$  point (dimensionality zero) detection elements. A woven fabric, on the other hand, provides a grid structure, out of linear (dimensionality one) fibres, which in turn can be used to localize an illumination point on a surface—but with detection elements of only order  $N$ . Moreover, by overlapping layers of this fabric, one could even ascertain the direction of incoming illumination. These fibres hence enable the realization of large-area optoelectronic functional surfaces. Thus, with the ability to interface materials with widely disparate electrical and optical properties in a fibre, achieve sub-micrometre features and realize arbitrary geometries over extended fibre lengths, we present the opportunity to deliver novel semiconductor device functionalities at fibre-optic length scales and cost. □

## Methods

### Glass synthesis

The amorphous semiconductor glass,  $\text{As}_{40}\text{Se}_{50}\text{Te}_{10}\text{Sn}_5$ , is prepared from high-purity As, Se, Te and Sn elements using sealed-ampoule melt-quenching techniques. The materials were weighed and placed into a quartz tube under a nitrogen atmosphere. The tube was heated to 330 °C for an hour at a rate of 1 °C  $\text{min}^{-1}$  under vacuum to remove surface oxides, and cooled to room temperature (23 °C) at the same rate. The ampoule was formed by sealing the tube under vacuum ( $\sim 10^{-3}$  torr). It was then heated to 800 °C at a rate of 2 °C  $\text{min}^{-1}$  in a rocking furnace, while being held vertical, for 24 h and then rocked for 6 h to increase mixing and homogenization. The glass liquid was cooled to 600 °C in the furnace, and then quenched in water. Subsequently, it was annealed for 30 min near the glass transition temperature,  $T_g = 180$  °C, before being cooled gradually to room temperature. Using this procedure, mechanically stable glass rods with diameter 12 mm and length 18 cm were obtained.

### Preform preparation and fibre drawing

The metal-core polymer-cladded fibre strands were obtained by drawing a preform with a 5-mm Sn (99.75% purity) core and 7.5-mm PES cladding. The preform was consolidated in a vacuum oven at 260 °C, and then drawn at  $\sim 305$  °C in a vertical tube furnace. Both ends of the preform were sealed with polymer to confine the metal during the consolidation and drawing processes. Metres of uniform metallic fibres with outer diameters from 500  $\mu\text{m}$  to 1.2 mm were successfully drawn and sectioned into strands. Sixty of these Sn strands were used in the construction of a macroscopic preform that yields the current hybrid fibre after drawing.

The dual electron-photon transport fibre preform was then assembled by wrapping a PEI film, coated on both sides with a layer of  $\text{As}_2\text{Se}_3$ , around a pyrex tube having 16-mm outer diameter. Specifically, a 2.6- $\mu\text{m}$ -thick layer of  $\text{As}_2\text{Se}_3$  was evaporated uniformly onto both sides of a 20-cm-wide, 8- $\mu\text{m}$ -thick, 1-m-long PEI film. An array of Sn strands were positioned around the outer surface of the multilayer structure by using a polymer solution of 20% PES, 80% N,N-dimethylacetamide. The resulting preform was then consolidated in a vertical rotating furnace at a temperature of 260 °C and a pressure of  $10^{-3}$  torr. In the furnace, the preform longitudinal axis is held vertically and a zone-refining heating process is carried out along the preform length. After consolidation, the preform was immersed in a liquid HF bath for 3 h to selectively etch away the pyrex tube in the centre, leaving a hollow core. The finalized preform was then drawn under the following conditions: a temperature of 302 °C, a downfeed speed of 0.003  $\text{mm s}^{-1}$ , and a capstan speed of 1  $\text{m min}^{-1}$ .

The spectroscopic fibre preform consists of an  $\text{As}_{40}\text{Se}_{50}\text{Te}_{10}\text{Sn}_5$  rod, having diameter 12 mm and length 18 cm, contacted by four Sn conduits, and surrounded by a quarter-wave  $\text{As}_2\text{Se}_3/\text{PEI}$  multilayer mirror structure with a  $\lambda/2$  PEI cavity and a protective PES cladding. The preform, 20 mm in diameter and 30 cm in length, was consolidated in a three-zone horizontal tube furnace while rotating the preform along its axis. Subsequently, the preform was drawn in a three-zone vertical tube furnace at a top zone temperature between 185 and 230 °C and a middle zone temperature of 295 °C with a tension of 500 g. A capstan speed of 0.7–3  $\text{m min}^{-1}$  produces a fibre of a diameter between about 1,200 and 500  $\mu\text{m}$  and a length of several hundred metres.

### Optical characterization

For optical characterization, we used a Verdi10 (Coherent) laser to pump a Ti-S femtosecond laser (Mira 900, Coherent). The femtosecond laser beam was then down-converted using an OPO (Mira OPO, Coherent). The OPO beam size was adjusted using a pinhole before passing through a beam splitter to allow collection of back-reflected light from the fibre. The beam emerging from the beam splitter was focused onto the outer surface of the fibre using a  $\times 5$  microscope objective ( $\text{NA} = 0.1$ ). The optical power incident on the fibre surface was maintained at 30 mW, using a variable optical attenuator, while the wavelength of the laser beam was swept. Back-reflected light through the beam splitter was detected using a Newport InGaAs photodetector (model 818-IG). For simultaneous electrical characterization, we measured the current flowing through the fibre electrodes using a pico-ampere meter/d.c. voltage source (Yokogawa/Hewlett Packard 4140B). The d.c. voltage difference applied to the two fibre electrodes was 50 V. At each wavelength, the incident optical power was adjusted, the electrical current was recorded, and the back-reflected light power measured.

Received 17 June; accepted 16 August 2004; doi:10.1038/nature02937.

1. Sze, S. M. *Semiconductor Devices: Physics and Technology* 2nd edn (John Wiley, New York, 2001).
2. Sedra, A. S. & Smith, K. C. *Microelectronic Circuits* (Oxford Univ. Press, Oxford, 2003).
3. Chuang, S. L. *Physics of Optoelectronic Devices* (John Wiley, New York, 1995).
4. Sanghera, J. S. & Aggarwal, I. D. (eds) *Infrared Fiber Optics* (CRC Press, New York, 1998).
5. Harrington, J. A. A review of IR transmitting, hollow waveguides. *Fiber Integrated Opt.* **19**, 211–227 (2000).
6. Katagiri, T., Matsuura, Y. & Miyagi, M. Metal-covered photonic bandgap multilayer for infrared hollow waveguides. *Appl. Opt.* **41**, 7603–7606 (2002).
7. Large, M. et al. Microstructured optical fibers: Why use polymers? *Proc. 29th Eur. Conf. on Opt. Comm. (ECOC'03 Rimini)*, 1014–1017 (2003); available at (<http://www.ofc.usyd.edu.au/?section=fibre&fibre=mpof#2>)
8. Broeng, J., Mogilevstev, D., Barkou, S. E. & Bjarklev, A. Photonic crystal fibers: A new class of optical waveguides. *Opt. Fiber Technol.* **5**, 305–330 (1999).
9. Eggleton, B. J., Kerbage, C., Westbrook, P. S., Windeler, R. S. & Hale, A. Microstructured optical fiber devices. *Opt. Express* **9**, 698–713 (2001).
10. van Eijkelenborg, M. A. et al. Microstructured polymer optical fiber. *Opt. Express* **9**, 319–327 (2001).
11. Allan, D. C. et al. in *Photonic Crystal and Light Localisation in the 21st Century* (ed. Soukoulis, C. M.) 305–320 (Kluwer Academic, Dordrecht, 2001).
12. Knight, J. C. Photonic crystal fibres. *Nature* **424**, 847–851 (2003).
13. Yeh, P., Yariv, A. & Marom, E. Theory of Bragg fiber. *J. Opt. Soc. Am.* **68**, 1196–1201 (1978).
14. Fink, Y. et al. A Dielectric omnidirectional reflector. *Science* **282**, 1679–1682 (1998).
15. Kuriki, K. et al. Hollow multilayer photonic bandgap fibers for NIR applications. *Opt. Express* **12**, 1510–1517 (2004).
16. Hart, S. D. et al. External reflection from omnidirectional dielectric mirror fibers. *Science* **296**, 510–513 (2002).
17. Temelkuran, B., Hart, S. D., Benoit, G., Joannopoulos, J. D. & Fink, Y. Wavelength-scalable hollow optical fibres with large photonic bandgaps for CO<sub>2</sub> laser transmission. *Nature* **420**, 650–653 (2002).

**Supplementary Information** accompanies the paper on [www.nature.com/nature](http://www.nature.com/nature).

**Acknowledgements** M.B. thanks P. H. Prideaux for teaching him optical fibre drawing. We also thank N. Orf for glass transition temperature measurements, Y. Kuriki for taking SEM micrographs, and K. Kuriki for providing PEI polymer films. This work was supported in part by DARPA/Carrano and DARPA/Griggs, DARPA QUIST, the ARO, the ONR, the AFOSR HEL-MURI, the US DOE, the ISN, and the Materials Research Science and Engineering Center (MRSEC) programme of the NSF (with the use of their Shared Experimental Facilities).

**Competing interests statement** The authors declare that they have no competing financial interests.

**Correspondence** and requests for materials should be addressed to Y.F. (yoel@mit.edu) or M.B. (mehmet@mit.edu).